Volume 1 | Number 1 | Jan 2013 | Pages 1–100

Journal of
Materials Chemistry A

Materials for energy and sustainability
www.rsc.org/materialsA

Li⁺

ROYAL SOCIETY OF CHEMISTRY

ROYAL SOCIETY OF CHEMISTRY

www.rsc.org/materialsA

One-pot synthesis of porous Pt-Au nanodendrites supported on reduced graphene oxide nanosheets toward catalytic reduction of 4-nitrophenol

Jing-Jing Lv,[a] Ai-Jun Wang,[a]* Xiaohong Ma,[b] Ru-Yi Xiang,[a] Jian-Rong Chen,[a] Jiu-Ju Feng,[a]*

[a] *College of Geography and Environmental Science, College of Chemistry and Life Science, Zhejiang Normal University, Jinhua 321004, China*

[b] *State Key Laboratory of Multiphase Complex Systems, Institute of Process Engineering, Chinese Academy of Sciences, Beijing 100190, China.*

Corresponding Author: Tel./Fax:+86 579 82282269. ajwang@zjnu.cn (AJW); jjfeng@zjnu.cn(JJF).

Abstract

In this work, a facile, convenient and effective one-pot wet-chemical method was developed for preparation of well-dispersed porous bimetallic Pt-Au alloyed nanodendrites uniformly supported on reduced graphene oxide nanosheets (Pt-Au pNDs/RGOs) at room temperature. The fabrication strategy was efficient and green by using cytosine as a structure-directing agent and a weak stabilizing agent, without employing any organic solvent, template, seed, surfactant, or complicated apparatus. The as-synthesized Pt-Au pNDs/RGOs exhibited significantly enhanced catalytic performances toward the reduction of 4-nitrophenol as compared to commercial Pt black and home-made Au nanocrystals.

Keywords: Nanodendrites; Pt-Au alloy; Reduced graphene oxide; 4-Nitrophenol

1. Introduction

As well known, 4-aminophenol (4-AP) has broad applications as photographic developer, hair-dying agent, anticorrosion-lubricant, and corrosion inhibitor.[1, 2] Furthermore, it is an important intermediate for preparation of a variety of analgesic and antipyretic drugs.[3, 4] Its synthesis is usually involved the reduction of 4-nitrophenol (4-NP) by sodium borohydride ($NaBH_4$) with the assistance of diverse catalysts such as iron acid,[5] metal oxide,[6] and especially metallic nanoparticles (NPs),[7, 8] because of their versatile, tunable size-, shape- and composition-dependent properties.[9, 10]

Particularly, noble metals including Pt, Pd, and Au have always attracted significant attention owing to their broad applications,[11-13] especially in catalysis.[14, 15] As a result, size- and shape-controlled synthesis of noble metal NPs recently stimulate tremendous research, and thereby various morphologies are fabricated such as wires,[16] rods,[17] prisms,[18] plates,[19] polyhedrons,[14] and branched nanostructures.[20]

Noble bimetallic nanocrystals (NCs) with highly branched structures have attracted increasing interest for their great potential applications in organic reactions,[21] fuel cells,[22] and sensing devices.[23] Accordingly, many synthetic approaches have been developed, such as hydrothermal method,[24] electrochemical deposition,[25] seed-mediated growth,[26] and galvanic replacement.[27] However, most of these demonstrations confront relatively time-consuming, high-cost, and complicated reaction steps.

It is desired to deposit bimetallic NCs on an appropriate support such as carbon-based materials, with the purpose to reduce their usage and prevent them from

further aggregation, sintering, or leaching.[28] Recently, graphene, as one of oxygen-abundant carbon layered materials, is extensively employed as a promising support for bimetallic catalysts, owing to its excellent mechanical, electrical, and thermal properties, along with its high specific surface area.[29] For example, Wang and co-workers fabricated three-dimensional Pt-on-Pd bimetallic nanodendrites supported on graphene as a catalyst for methanol oxidation.[22] He and co-workers synthesized Au-Pd NPs/graphene oxide, which exhibited excellent catalytic activity for the reduction of 4-NP to 4-AP.[30]

Herein, we report a facile and convenient wet-chemical route to synthesize porous Pt-Au nanodendrites with highly branched nanostructures uniformly supported on reduced graphene oxide nanosheets (denoted as Pt-Au pNDs/RGOs). The catalytic activity of the as-prepared nanocomposites was examined toward the reduction reaction of 4-NP in the presence of $NaBH_4$.

2. Experimental section

2.1 Chemicals

Chloroplatinic acid ($H_2PtCl_6·6H_2O$), chloroauric acid ($HAuCl_4$), cytosine, hydrazine hydrate (16.5 M), graphite powder, 4-nitrophenol (4-NP), sodium borohydride ($NaBH_4$), and commercial Pt black were purchased from Shanghai Aladdin Chemical Reagent Company (Shanghai, China). All the other chemicals were analytical grade and used without further purification. All the aqueous solutions were prepared with twice-distilled water.

2.2 Synthesis of Pt-Au pNDs/RGOs

In a typical synthesis, GOs were firstly prepared by the modified Hummer's method.[31] Afterward, 2.9 mL of H_2PtCl_6 (38.6 mM), 2 mL of $HAuCl_4$ (24.3 mM), and 0.028 g cytosine (25 mM) were put into 10 mL solution containing 1 mM GOs under stirring. Next, the pH value of the mixed solution was adjusted to 12 by using freshly prepared 0.1 M NaOH. Then, the mixture was placed into the water-bath (25 °C) and immediately turned black upon the addition of 100 μL hydrazine hydrate under stirring, followed by continually reacting for another 1 h. Finally, the black precipitate was collected by centrifugation, thoroughly washed with ethanol and water, and dried at 60 °C in a vacuum for further characterization.

In control experiments, Au NCs were fabricated in a similar way, as described previously.[32] Moreover, the control experiments were carried out by changing the amount of cytosine or preparing without GOs, while the other experimental conditions were kept the same.

2.3 Characterization

The morphology, composition, and crystal structures of the samples were characterized by transmission electron microscope (TEM), high-resolution TEM (HRTEM) images, X-ray energy dispersive spectrum (EDS), and high angle annular dark field-scanning transmission electron microscopy (HAADF-STEM) on a JEM-2100F HR transmission electron microscope coupled with an energy-dispersive X-ray spectrometer (Oxford-1NCA). TEM analysis was conducted at an accelerating

voltage of 200 kV, and Cu grids were used as substrates. A small amount of the black

sample was dispersed in ethanol under ultrasonication, and then a drop of the

suspension was dropped onto the Cu grid for TEM observation.

The crystal structures were performed by X-ray diffraction (XRD) on a

Bruker-D8-AXS diffractometer system equipped with Cu Kα radiation (Bruker Co.,

Germany). And X-ray photoelectron spectroscopy (XPS) measurements were

conducted by a thermofisher-ESCALab 250 (ThermoFisher, E. Grinstead, UK), using

Al Kα X-ray radiation (1486.6 eV) for excitation. Raman spectra were recorded on a

Renishaw Raman system model 1000 spectrometer equipped with a charge-coupled

device (CCD) detector. Thermogravimetric analysis (TGA) was done under a flow of

air on a NETZSCH STA 449C analyzer. The samples were heated from 25 to 900 °C

with a heat rate of 10 °C min^{-1}.

2.4 Catalytic measurements

The measurements for catalytic reduction of 4-NP by Pt-Au pNDs/RGOs, Pt

black, and Au NCs were conducted by UV-Vis spectroscopy in a quartz cuvette on a

Lambda 950 UV/Vis/NIR spectrophotometer (Perkin Elmer Corporation). A total

amount of 300 μL of 4-NP (0.7 mM) was diluted with 1 mL of water, followed by the

addition of 1 mL of freshly prepared ice-cold $NaBH_4$ solution (0.5 M). Subsequently,

a certain amount of the as-prepared catalyst suspension was injected into the cuvette

to trigger the reaction, and monitored the UV-Vis spectral changes at different time

intervals. All of the experiments were conducted at room temperature, if not stated

otherwise.

3. Results and discussion

As illustrated in Fig. 1A, the typical product contains a lot of nanodendrites uniformly anchored on RGOs (labeled with red arrows). The as-prepared nanodendrites possess interconnected porous structures (Fig. 1B, C), and their size is ranging from 51 to 91 nm in diameter, with an average diameter of 70 nm (inset in Fig. 1B).

The selected-area electron diffraction (SAED) pattern displays the characteristic of the face-centered cubic (fcc) feature of Pt/Au (inset in Fig. 1C), revealing polycrystalline nature of the as-synthesized Pt-Au nanodendrites.[33] Moreover, their highly crystalline is strongly demonstrated by HRTEM image taken from the marked region (Fig. 1D), in which well-defined lattice fringes are observed, with the interplanar spacing distances of 0.237 and 0.193 nm, which are matched well with the (111) and (200) crystal planes, respectively.[34, 35]

The chemical composition and elemental distribution of Pt-Au pNDs/RGOs were characterized by EDS-mapping (Fig. 2A-E) and EDS spectrum (Fig. 2F). The porous interconnected dendritic structures of Pt-Au pNDs can be clearly observed in HAADF-STEM image (Fig. 2A). And the homogeneous distribution of Pt and Au elements throughout the whole Pt-Au pNDs is confirmed by the respective elemental mapping images (Fig. 2B-D). It means the alloyed feature of Pt-Au pNDs,[36] as further demonstrated by the line scanning profiles (Fig. 2E),[37] where Pt and Au are homogeneously distributed in an individual nanodendrite. The Pt/Au atomic ratio is

50.6:49.4 based on the data from the line scanning profiles and EDS spectrum (Fig.

2F). This value is in good agreement with the initial ratio of the precursors

(H_2PtCl_6:$HAuCl_4$ = 50:50), showing the effective reduction strategy in the preparation

of Pt-Au pNDs.

XRD pattern of Pt-Au pNDs/RGOs (Fig. 3A, curve a) was performed to provide

more structural information, using GOs as a reference (Fig. 3A, curve b). As

illustrated, there are four representative diffraction peaks emerged at 38.8°, 44.9°,

65.9°, and 79.4° for Pt-Au pNDs/RGOs, which are indexed to the (111), (200), (220),

and (311) planes of the fcc structure of Pt/Au metal.[38] It's worth noting that these

peaks are coincidently located between bulk Pt (JCPDS 04-0802) and Au (JCPDS

04-0784), further confirming the formation of uniform Pt-Au alloy.[39] Additionally,

unlike Pt-Au pNDs/RGOs, there is a sharp peak located at 10.8° for GOs, which is

assigned to the (001) planes of graphite oxide.[40] The difference is ascribed to the

significant reduction of GOs and the exfoliation of the layered graphene.[41]

This conclusion is strongly supported by Raman spectrum of Pt-Au pNDs/RGOs

(Fig. 3B, curve a), using GOs as a standard (Fig. 3B, curve b). Clearly, there are two

predominant peaks at ca. 1610 and 1350 cm^{-1}, which correspond to well-documented

G and D bands.[42] The G band is associated with the vibrations of the graphite sp^2

carbon domains, while the D band comes from the vibrations of the sp^3 carbon atoms

in the disordered graphene nanosheets.[43] The D/G intensity ratio (I_D/I_G) is usually

used as an indicator for quantifying the level of chemical modification of the graphitic

carbon sample.[44] The I_D/I_G value is 1.1 for Pt-Au pNDs/RGOs, which is higher than

that of GOs (0.9), demonstrating the efficient removal of oxygenated functional groups from GOs during the present synthesis.[45]

XPS analysis further verified the efficient removal of oxygenated functional groups from GOs and the formation of Pt-Au pNDs/RGOs (Fig. 4). Specifically, there are four representative peaks located at 284.7, 285.6, 286.5, and 288.3 eV in the high-resolution C 1s spectrum (Fig. 4A), which are attributed to the C-C, C-O, C=O and O-C=O groups, respectively.[46] Impressively, the intensity of C-C band is much higher than that of GOs (Fig. S1), revealing that the oxygenated functional groups are effectively reduced in the reaction, causing the formation of many defects on RGOs. These defects would provide binding sites for subsequent deposition of Pt-Au pNPs.[47]

The surface chemical states of Pt and Au were analyzed by the Pt 4f (Fig. 4B) and Au 4f (Fig. 4C) XPS spectra. The strong doublet peaks of Pt 4f are emerged at 71.0 and 74.4 eV, which is ascribed to Pt^0, whereas nearly no peaks are detected at 72.6 and 75.7 eV, showing the complete reduction of Pt^{2+} to Pt^0 during the reaction.[48] Meanwhile, the predominant Au^0 $4f_{5/2}$ and Au^0 $4f_{7/2}$ peaks illustrate that $HAuCl_4$ is efficiently reduced to metallic Au^0.[49] These observations reveal that Pt^0 and Au^0 are the predominant species in Pt-Au pNDs/RGOs.

The amount of cytosine played a key role in the formation of Pt-Au nanocrystals (Fig. 5). The absence of cytosine yields numerous irregular nanoparticles with severe aggregation (Fig. 5A). Less cytosine (10 mM) results in the emergence of immature dendritic Pt-Au nanocrystals with broad size distribution (Fig. 5B), and the best ones are obtained in the case of 25 mM cytosine (Fig. 1A, B). Nevertheless, excessive

8

cytosine such as 50 mM (Fig. 5C) induces the formation of irregular dendritic Pt-Au nanocrystals with low surface coverage and reduced particle size in contrast to the case of 25 mM cytosine, reflecting that cytosine acts as a structure-directing agent and a weak stabilizing agent.

Cytosine molecules selectively interacted and adsorbed on the Pt and Au nuclei with the different crystal planes.[50] Specifically, the crystal growth was severely blocked on the high energy crystal planes, such as (110) and (100) crystal planes, which was bound by the adsorbed molecules.[51] While the growth on the (111) crystal planes with low energy was promoted according to the direct growth mechanism,[20, 36] as confirmed by the XRD pattern shown in the Fig. 3A, resulting in the formation of dendritic nanostructures. Moreover, the presence of cytosine could also act as a physical barrier to hinder the nanocrystals to aggregate and thus improve their dispersity.[52, 53]

Moreover, the absence of GOs leads to the formation of seriously aggregated Pt-Au dendritic products (Fig. S2), indicating that GOs are responsible for the well distribution of Pt-Au products as a support in the present synthesis. This is attributed to the fact that many oxygenated functional groups on GOs surfaces control the reduction kinetics.[49]

The catalytic properties of Pt-Au pNDs/RGOs were examined via the reduction reaction of 4-NP to 4-AP in the presence of excess $NaBH_4$, as depicted in Fig. 6. BH_4^- would adsorb onto the catalyst surface and transfer active hydrogen species to the particle surface to form metal hydride complex.[54] Meanwhile, 4-NP also adheres to

the surfaces of Pt-Au pNDs/RGOs via chemical adsorption.[55] As a result, the adsorbed

hydrogen species would transfer to nitro groups, inducing the reduction of nitro

groups to amino groups, as strongly supported by the previous work.[56, 57]

The reduction processes of 4-NP were monitored by UV-Vis spectroscopy at

different time intervals and dosage, using Pt-Au pNDs/RGOs as a catalyst (Fig. 7A-C).

It is known that this reaction is difficult to proceed without a catalyst.[58] The

absorption peak intensities at 400 nm were used to quantify the reduction

concentration of 4-NP by extending the reaction time. After the addition of Pt-Au

pNDs/RGOs to the mixed solution of 4-NP and $NaBH_4$, the absorption peak at 400

nm significantly decreases as the reaction proceeds, owing to the reduction of 4-NP.[7]

Simultaneously, a new peak appears at 300 nm, accompanied with the increase of the

peak intensity, which is ascribed to the formation of 4-AP.[59] In addition, increasing the

dosage of Pt-Au pNDs/RGOs facilitates the reduction reaction, in which the solution

color is changed from yellowish green to colorless within 10 min by using 50 μL

Pt-Au pNDs/RGOs with the concentration of 0.1 mg mL^{-1} (Fig. 7C).

For comparison, the catalytic performance of commercial Pt black (1 mg mL^{-1})

and home-made Au NCs (1 mg mL^{-1}) were investigated under the identical conditions.

However, the reaction time is 1.0 h for Pt black (Fig. S3A) and 2.5 h for home-made

Au NCs (Fig. S3B), respectively. With respect to the conversion of 4-NP (Fig. 6D),

the catalytic activity is significantly improved for Pt-Au pNDs/RGOs in contrast to Pt

black and Au NCs.

Fig. 8 shows the logarithm plot of the absorbance $(-\ln(A/A_0))$ with reaction time

to further examine the catalytic activity of Pt-Au pNDs/RGOs, using Pt black and Au NCs as references. The apparent kinetic rate constant (k_{app}) is proportional to the total surface area of a catalyst, which can be estimated based on the regression of the slope from the logarithm plot ($-dC_t/d_t=k_{app}C_t$).[60] As listed in Table 1, the k_{app} value is 3.8×10^{-3} s^{-1} for Pt-Au pNDs/RGOs. This value is about 5-fold and 12-fold higher than those of Pt black (0.7×10^{-3} s^{-1}) and Au NCs (0.3×10^{-3} s^{-1}), evidencing the enhanced catalytic acitivity of Pt-Au pNDs/RGOs.

Meanwhile, the normalized rate constant (k_{nor}) was also provided, which was associated with the amount of a catalyst, i.e., $k_{nor}=k_{app}/m$. Herein, TGA analysis demonstrated that Pt and Au loading was measured to be 81.4 wt % in Pt-Au pNDs/RGOs, owing to the presence of RGOs (Fig. S4).[61] As shown in Table 1, the k_{nor} value of Pt-Au pNDs/RGOs (926 s^{-1} g^{-1}) is much higher than those of Pt black (15 s^{-1} g^{-1}) and Au NCs (6 s^{-1} g^{-1}). At the same time, the k_{app} and k_{nor} values of Pt-Au pNDs/RGOs is comparable among those catalysts in the literature (Table S1), including Pt$_{55}$Pd$_{38}$Bi$_7$ nanowires (k_{nor}=286 s^{-1} g^{-1}),[62] AuPd nanocrystals (k_{nor}=78 s^{-1} g^{-1}),[63] PtNi nanoparticles (k_{nor}=483 s^{-1} g^{-1}),[64] and Fe@Au-ATPGO (k_{nor}=400 s^{-1} g^{-1}).[65] These results strongly reveal the improved catalytic activity of Pt-Au pNDs/RGOs.

Interestingly, the dosage of Pt-Au pNDs/RGOs is 10 times less than those of Pt black and Au NCs, while it needs much less reaction time to achieve the same conversion quantity of 4-NP. The above results verify the enhanced catalytic performance of Pt-Au pNDs/RGOs, owing to the unique interconnected

nanostructures of Pt-Au pNDs for providing more active sites available,[58] the improved mass transport by using RGOs as a support,[66] along with the synergistic effects between Pt and Au.[67]

4. Conclusions

In conclusion, we have prepared Pt-Au pNDs/RGOs through an efficient co-reduction wet-chemical route at room temperature. The co-existence of cytosine and GOs plays crucial roles for the growth of Pt-Au pNDs with high quality. The as-prepared Pt-Au pNDs/RGOs show improved catalytic activity for the reduction of 4-NP to 4-AP, compared with commercial Pt black and home-made Au NCs. It's believed that the as-prepared Pt-Au pNDs/RGOs will be used as a promising catalyst for applying in organic synthesis or other fields.

References

1 P. Deka, R. C. Deka and P. Bharali, *New J. Chem.*, 2014, **38**, 1789-1793.

2 J. Li, C.-y. Liu and Y. Liu, *J. Mater. Chem.*, 2012, **22**, 8426-8430.

3 T. R. Mandlimath and B. Gopal, *J. Mol. Catal. A: Chem.*, 2011, **350**, 9-15.

4 K.-L. Wu, X.-W. Wei, X.-M. Zhou, D.-H. Wu, X.-W. Liu, Y. Ye and Q. Wang, *J.*

Phys. Chem. C, 2011, **115**, 16268-16274.

5 H. Lu, H. Yin, Y. Liu, T. Jiang and L. Yu, *Catal. Commun.*, 2008, **10**, 313-316.

6 R. Rahimi, S. Safalou Moghaddam and M. Rabbani, *J. Sol-Gel Sci. Technol.*, 2012, **64**, 17-26.

7 Y. Liu, Z. Fang, L. Kuai and B. Geng, *Nanoscale*, 2014, **6**, 9791-9797.

8 J. A. Johnson, J. J. Makis, K. A. Marvin, S. E. Rodenbusch and K. J. Stevenson, *J. Phys. Chem. C*, 2013, **117**, 22644-22651.

9 J. Zheng, Y. Dong, W. Wang, Y. Ma, J. Hu, X. Chen and X. Chen, *Nanoscale*, 2013, **5**, 4894-4901.

10 A. Gangula, R. Podila, R. M, L. Karanam, C. Janardhana and A. M. Rao, *Langmuir*, 2011, **27**, 15268-15274.

11 Z. Jin, M. Xiao, Z. Bao, P. Wang and J. Wang, *Angew. Chem. Int. Ed.*, 2012, **51**, 6406-6410.

12 S. Sahu, A. Samantara, A. Dash, R. R. Juluri, R. Sahu, B. K. Mishra and B. Jena, *Nano Res.*, 2013, **6**, 635-643.

13 A. Chen and P. Holt-Hindle, *Chem. Rev.*, 2010, **110**, 3767-3804.

14 K. Zhou and Y. Li, *Angew. Chem. Int. Ed.*, 2012, **51**, 602-613.

15 W. Si, J. Li, H. Li, S. Li, J. Yin, H. Xu, X. Guo, T. Zhang and Y. Song, *Nano Res.*, 2013, **6**, 720-725.

16 S. Guo, D. Li, H. Zhu, S. Zhang, N. M. Markovic, V. R. Stamenkovic and S. Sun, *Angew. Chem. Int. Ed.*, 2013, **52**, 3465-3468.

17 Y. Lu, Y. Jiang and W. Chen, *Nano Energy*, 2013, **2**, 836-844.

18 F. Lu, Y. Zhang, L. Zhang, Y. Zhang, J. X. Wang, R. R. Adzic, E. A. Stach and O. Gang, *J. Am. Chem. Soc.*, 2011, **133**, 18074-18077.

19 B. Sadeghi, M. A. S. Sadjadi and R. A. R. Vahdati, *Superlattices Microstruct.*, 2009, **46**, 858-863.

20 B. Lim and Y. Xia, *Angew. Chem. Int. Ed.*, 2011, **50**, 76-85.

21 J. Xu, A. R. Wilson, A. R. Rathmell, J. Howe, M. Chi and B. J. Wiley, *ACS Nano*, 2011, **5**, 6119-6127.

22 S. Guo, S. Dong and E. Wang, *ACS Nano*, 2009, **4**, 547-555.

23 W. He, X. Wu, J. Liu, X. Hu, K. Zhang, S. Hou, W. Zhou and S. Xie, *Chem. Mater.*, 2010, **22**, 2988-2994.

24 J.-N. Zheng, L.-L. He, F.-Y. Chen, A.-J. Wang, M.-W. Xue and J.-J. Feng, *J. Mater. Chem. A*, 2014, **2**, 12899-12906.

25 C. Koenigsmann, A. C. Santulli, K. Gong, M. B. Vukmirovic, W.-p. Zhou, E. Sutter, S. S. Wong and R. R. Adzic, *J. Am. Chem. Soc.*, 2011, **133**, 9783-9795.

26 B. Lim, M. Jiang, P. H. C. Camargo, E. C. Cho, J. Tao, X. Lu, Y. Zhu and Y. Xia, *Science*, 2009, **324**, 1302-1305.

27 H. Zhang, M. Jin, J. Wang, W. Li, P. H. C. Camargo, M. J. Kim, D. Yang, Z. Xie and Y. Xia, *J. Am. Chem. Soc.*, 2011, **133**, 6078-6089.

28 R. Ning, J. Tian, A. M. Asiri, A. H. Qusti, A. O. Al-Youbi and X. Sun, *Langmuir*, 2013, **29**, 13146-13151.

29 J.-N. Zheng, J.-J. Lv, S.-S. Li, M.-W. Xue, A.-J. Wang and J.-J. Feng, *J. Mater. Chem. A*, 2014, **2**, 3445-3451.

30 Y. He, N. Zhang, L. Zhang, Q. Gong, M. Yi, W. Wang, H. Qiu and J. Gao, *Mater. Res. Bull.*, 2014, **51**, 397-401.

31 W. S. Hummers and R. E. Offeman, *J. Am. Chem. Soc.*, 1958, **80**, 1339-1339.

32 Y.-Q. Dang, H.-W. Li, B. Wang, L. Li and Y. Wu, *ACS Appl. Mat. Interfaces*, 2009, **1**, 1533-1538.

33 L. Wang and Y. Yamauchi, *Chem. Mater.*, 2009, **21**, 3562-3569.

34 A.-X. Yin, X.-Q. Min, Y.-W. Zhang and C.-H. Yan, *J. Am. Chem. Soc.*, 2011, **133**, 3816-3819.

35 W. Zhang, J. Yang and X. Lu, *ACS Nano*, 2012, **6**, 7397-7405.

36 X. Huang, E. Zhu, Y. Chen, Y. Li, C.-Y. Chiu, Y. Xu, Z. Lin, X. Duan and Y. Huang, *Adv. Mater.*, 2013, **25**, 2974-2979.

37 Z.-C. Zhang, J.-F. Hui, Z.-G. Guo, Q.-Y. Yu, B. Xu, X. Zhang, Z.-C. Liu, C.-M. Xu, J.-S. Gao and X. Wang, *Nanoscale*, 2012, **4**, 2633-2639.

38 S. Zhang, Y. Shao, H.-g. Liao, J. Liu, I. A. Aksay, G. Yin and Y. Lin, *Chem. Mater.*, 2011, **23**, 1079-1081.

39 Y. Lu, Y. Jiang, H. Wu and W. Chen, *J. Phys. Chem. C*, 2013, **117**, 2926-2938.

40 Q.-L. Zhang, T.-Q. Xu, J. Wei, J.-R. Chen, A.-J. Wang and J.-J. Feng, *Electrochim. Acta*, 2013, **112**, 127-132.

41 J. Li, W. Tang, J. Huang, J. Jin and J. Ma, *Catal. Sci. Technol.*, 2013, **3**, 3155-3162.

42 S.-S. Li, J.-N. Zheng, X. Ma, Y.-Y. Hu, A.-J. Wang, J. Chen and J.-J. Feng, *Nanoscale*, 2014, **6**, 5708-5713.

43 M. Liu, Y. Lu and W. Chen, *Adv. Funct. Mater.*, 2013, **23**, 1289-1296.

44 J. Tian, S. Liu, Y. Zhang, H. Li, L. Wang, Y. Luo, A. M. Asiri, A. O. Al-Youbi and X. Sun, *Inorg. Chem.*, 2012, **51**, 4742-4746.

45 S. Liu, L. Wang, J. Tian, W. Lu, Y. Zhang, X. Wang and X. Sun, *J. Nanopart. Res.*, 2011, **13**, 4731-4737.

46 J.-J. Lv, S.-S. Li, A.-J. Wang, L.-P. Mei, J.-R. Chen and J.-J. Feng, *Electrochim. Acta*, 2014, **136**, 521-528.

47 L. Li, M. Chen, G. Huang, N. Yang, L. Zhang, H. Wang, Y. Liu, W. Wang and J. Gao, *J. Power Sources*, 2014, **263**, 13-21.

48 G. Fu, X. Jiang, M. Gong, Y. Chen, Y. Tang, J. Lin and T. Lu, *Nanoscale*, 2014, **6**, 8226-8234.

49 X.-R. Li, X.-L. Li, M.-C. Xu, J.-J. Xu and H.-Y. Chen, *J. Mater. Chem. A*, 2014, **2**, 1697-1703.

50 Z.-Y. Lv, A.-Q. Li, Y. Fei, Z. Li, J.-R. Chen, A.-J. Wang and J.-J. Feng, *Electrochim. Acta*, 2013, **109**, 136-144.

51 M. Chen, B. Wu, J. Yang and N. Zheng, *Adv. Mater.*, 2012, **24**, 862-879.

52 G. Fu, K. Wu, J. Lin, Y. Tang, Y. Chen, Y. Zhou and T. Lu, *J. Phys. Chem. C*, 2013, **117**, 9826-9834.

53 Z. Niu and Y. Li, *Chem. Mater.*, 2013, **26**, 72-83.

54 H.-Z. Zhu, Y.-M. Lu, F.-J. Fan and S.-H. Yu, *Nanoscale*, 2013, **5**, 7219-7223.

55 Y. Choi, H. S. Bae, E. Seo, S. Jang, K. H. Park and B.-S. Kim, *J. Mater. Chem.*, 2011, **21**, 15431-15436.

56 L. Ai, H. Yue and J. Jiang, *J. Mater. Chem.*, 2012, **22**, 23447-23453.

57 W. Lu, R. Ning, X. Qin, Y. Zhang, G. Chang, S. Liu, Y. Luo and X. Sun, *J. Hazard. Mater.*, 2011, **197**, 320-326.

58 Q. Ji, J. P. Hill and K. Ariga, *J. Mater. Chem. A*, 2013, **1**, 3600-3606.

59 N. Zhang and Y.-J. Xu, *Chem. Mater.*, 2013, **25**, 1979-1988.

60 W. Ye, Y. Chen, F. Zhou, C. Wang and Y. Li, *J. Mater. Chem.*, 2012, **22**, 18327-18334.

61 J.-N. Zheng, S.-S. Li, X. Ma, F.-Y. Chen, A.-J. Wang, J. Chen and J.-J. Feng, *J. Mater. Chem. A*, 2014, **2**, 8386-8395.

62 Y.-Y. Shen, Y. Sun, L.-N. Zhou, Y.-J. Li and E. S. Yeung, *J. Mater. Chem. A*, 2014, **2**, 2977-2984.

63 J. Zhang, C. Hou, H. Huang, L. Zhang, Z. Jiang, G. Chen, Y. Jia, Q. Kuang, Z. Xie and L. Zheng, *Small*, 2013, **9**, 538-544.

64 S. K. Ghosh, M. Mandal, S. Kundu, S. Nath and T. Pal, *Appl. Catal., A*, 2004, **268**, 61-66.

65 V. K. Gupta, N. Atar, M. L. Yola, Z. Üstündağ and L. Uzun, *Water Res.*, 2014, **48**, 210-217.

66 J.-J. Lv, J.-N. Zheng, L.-L. Chen, M. Lin, A.-J. Wang, J.-R. Chen and J.-J. Feng, *Electrochim. Acta*, 2014, **143**, 36-43.

67 Y. Yamauchi, A. Tonegawa, M. Komatsu, H. Wang, L. Wang, Y. Nemoto, N. Suzuki and K. Kuroda, *J. Am. Chem. Soc.*, 2012, **134**, 5100-5109.

Caption

Fig. 1 Low (A), medium (B), and high magnification (C, D) TEM images of Pt-Au

pNDs/RGOs. Insets in (B) and (C) show the corresponding size-distribution

histogram and SAED pattern. The products were obtained with 25 mM cytosine.

Fig. 2 HAADF-STEM (A), HAADF-STEM-EDS mapping (B-D) images, line

scanning profiles (E), and EDS spectrum (F) of Pt-Au pNDs/RGOs.

Fig. 3 (A) XRD and (B) Raman spectra of Pt-Au pNDs/RGOs.

Fig. 4 High-resolution C 1s (A), Pt 4f (B), and Au 4f (C) XPS spectra of Pt-Au

pNDs/RGOs.

Fig. 5 TEM images of the products prepared without (A), and with 10 mM (B) and 50

mM (C) cytosine.

Fig. 6 Schematic illustration for the reduction of 4-NP.

Fig. 7 Time-dependent UV-Vis spectra of 4-NP catalyzed by different dosage of Pt-Au

pNDs/RGOs (0.1 mg mL^{-1}): 10 μL (A), 25 μL (B), and 50 μL (C). The conversion of

4-NP with reaction time in the presence of 0.005 mg Pt-Au pNDs/RGOs (curve a),

0.05 mg Pt black (curve b), and 0.05 mg Au NCs (curve c), respectively.

Fig. 8 The plots of $-\ln(A/A_0)$ against the reaction time for the reduction of 4-NP catalyzing by Pt-Au pNDs/RGOs (curve a), Pt black (curve b), and Au NCs (curve c), respectively.

Table 1 Comparison of the catalytic performances of Pt-Au pNDs/RGOs, Pt black, and Au NCs for the reduction of 4-NP under the identical conditions.

Figures

Fig. 1
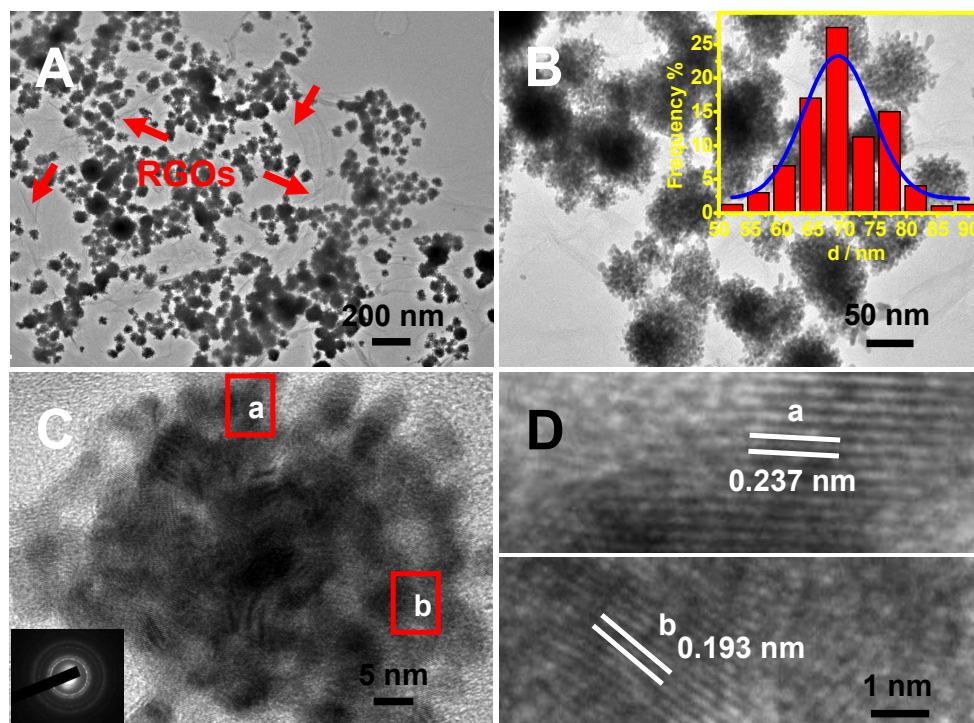
Fig. 2
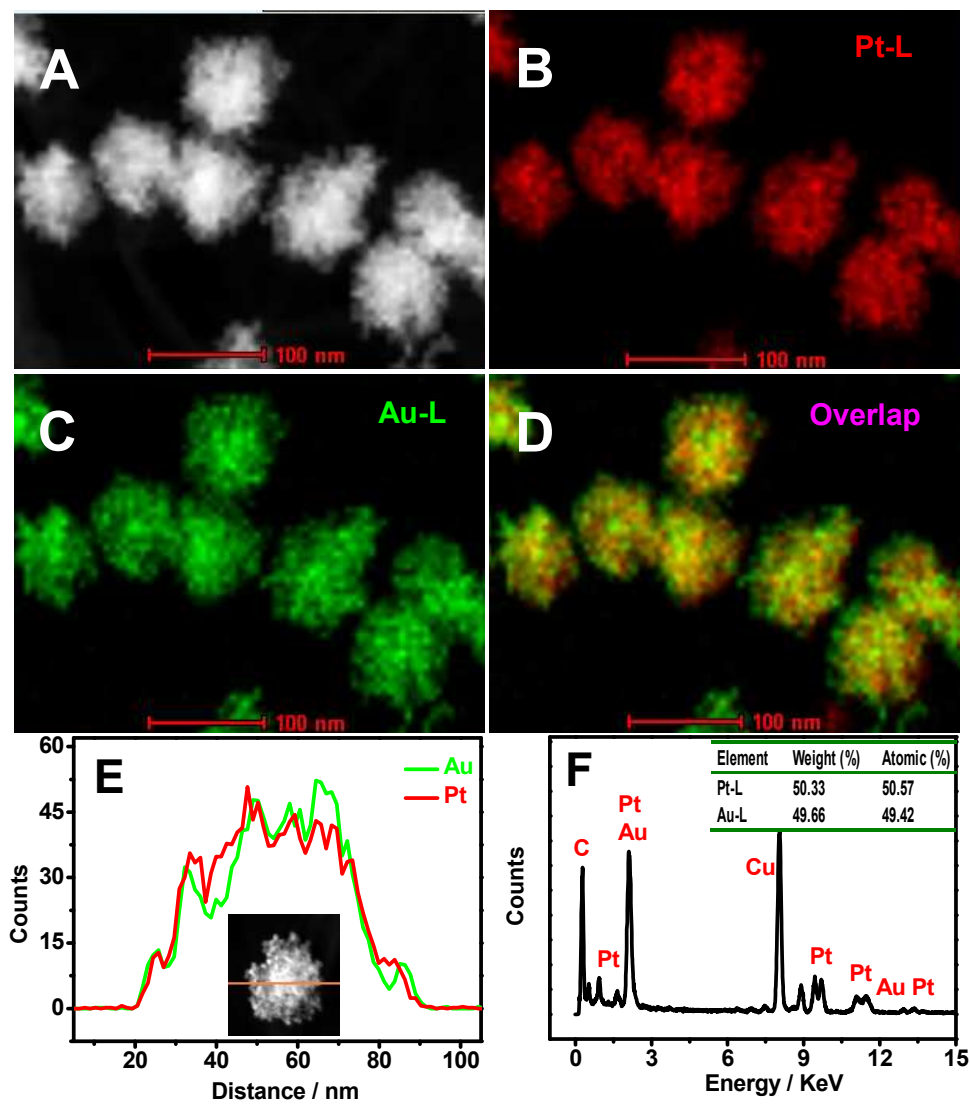
Fig. 3
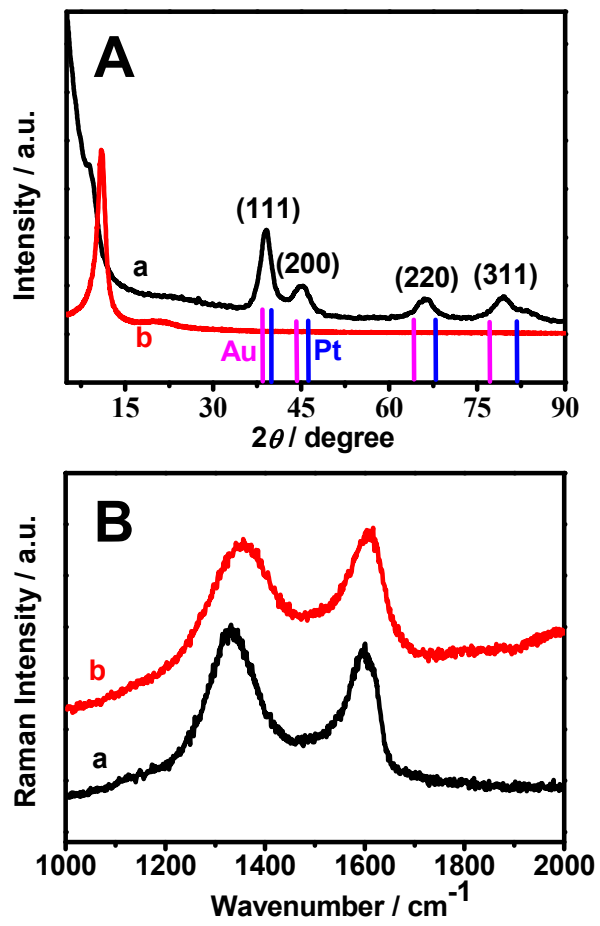
Fig. 4
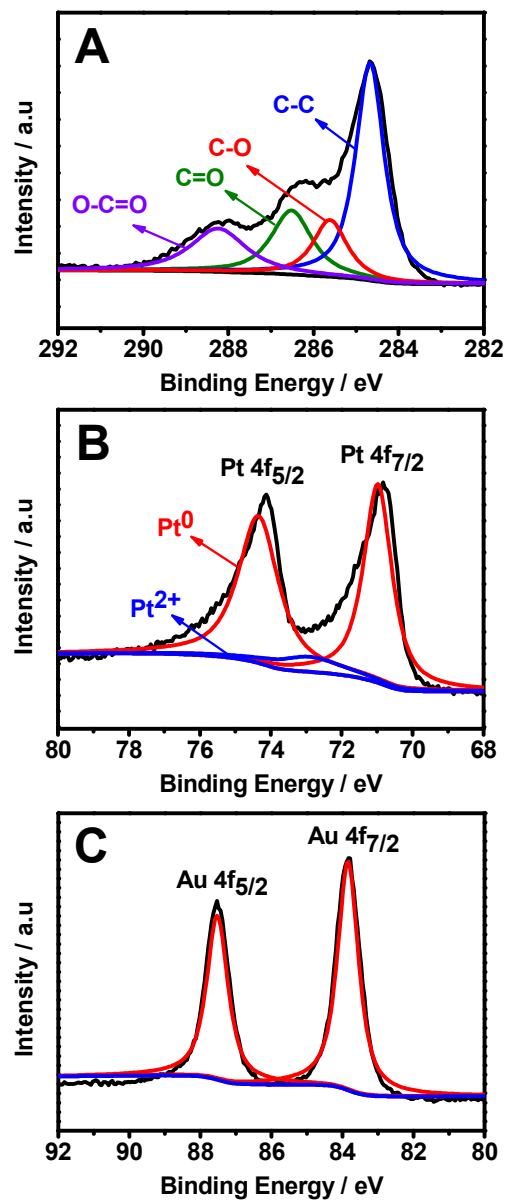
Fig. 5
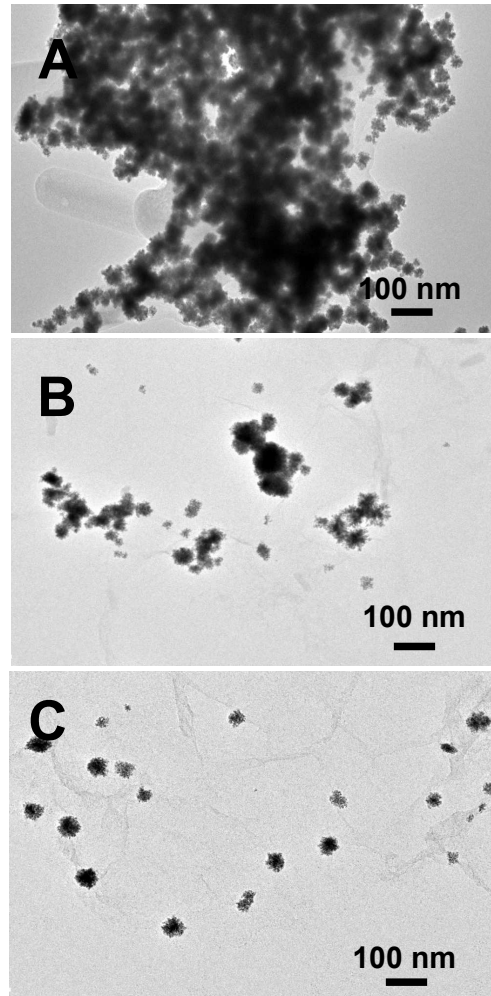
Fig. 6
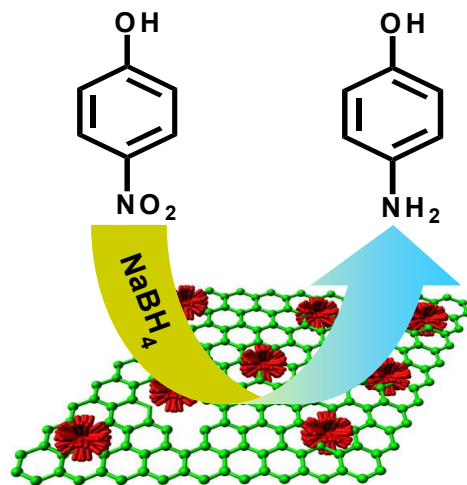
Fig. 7
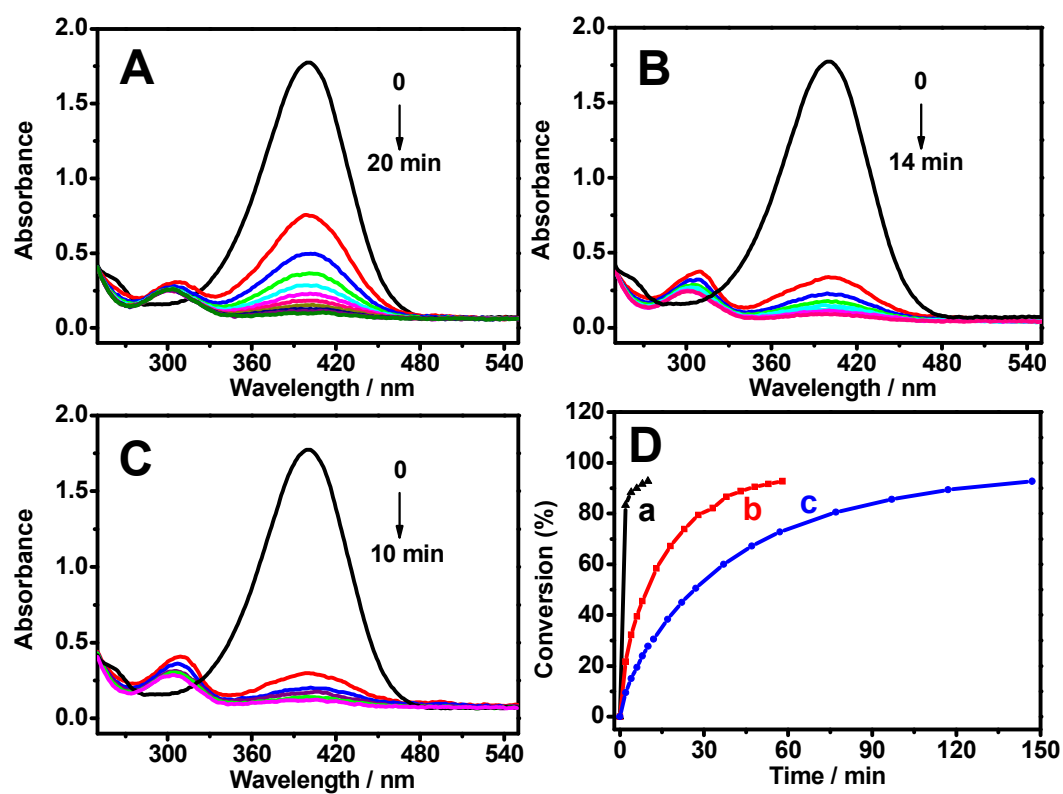
Fig. 8
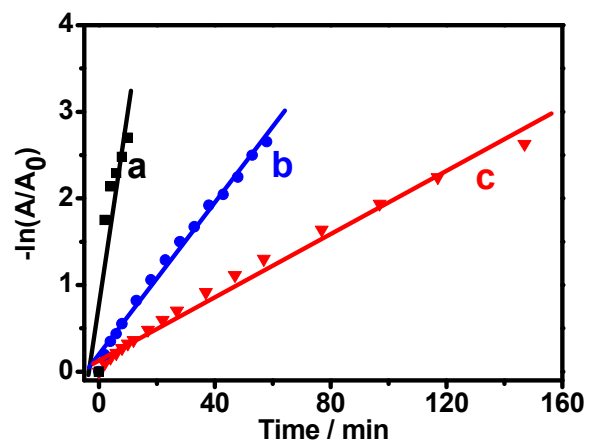
Table 1

Catalysts	k_{app} ($\times 10^{-3}$ s^{-1})	k_{nor} (s^{-1} g^{-1})	Time (min)
Pt-Au pNDs/RGOs	3.8	926	10
Pt black	0.7	15	58
Au NCs	0.3	6	147

Graphical Abstract
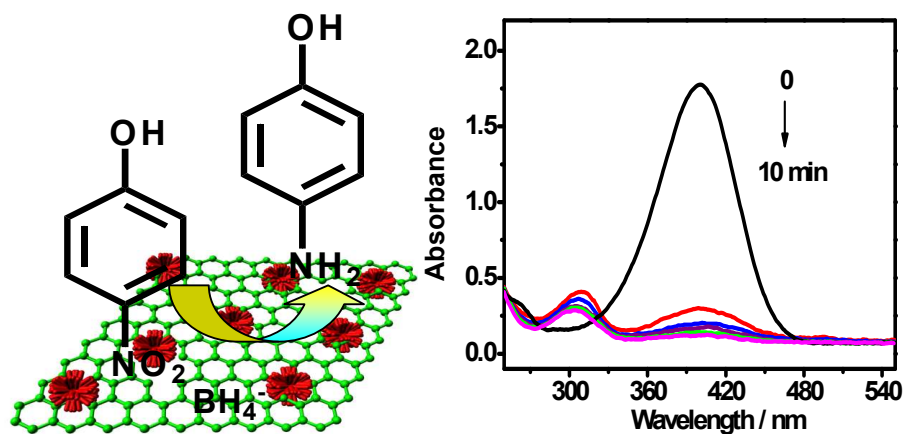
A simple, facile, green and effective one-pot wet-chemical co-reduction method was developed for preparation of Pt-Au pNDs/RGOs in the presence of cytosine as a structure-directing agent and a weak stabilizing agent. The nanocomposites exhibited significantly enhanced catalytic performance towards 4-nitrophenol reduction.